

1 Uranium isotope evidence for an expansion of anoxia in terminal 2 Ediacaran oceans

3
4 Rosalie Tostevin^{1,2*}, Matthew O Clarkson³, Sophie Gangl³, Graham A Shields⁴,
5 Rachel A Wood⁵, Fred Bowyer⁵, Amelia M Penny⁵, Claudine H Stirling³

6
7 ¹University of Otago, Department of Geology, Dunedin 9016, New Zealand

8 ²University of Oxford, Department of Earth Science, Oxford, UK, OX1 3AN

9 ³University of Otago, Centre for Trace Element Analysis and Department of

10 Chemistry, Union Place West, Dunedin 9016, New Zealand

11 ⁴University College London, Department of Earth Sciences, Gower Street, London,

12 UK, WC1E 6BT

13 ⁵The University of Edinburgh, School of GeoSciences, James Hutton Road,

14 Edinburgh, EH9 3FE

15 *Corresponding author: Rosalie.tostevin@earth.ox.ac.uk

16
17 Keywords: redox; uranium; Ediacaran; oxygen; animals

18 **Abstract**

19 Anoxic and iron-rich oceanic conditions prevailed throughout most of the Archean

20 and Proterozoic (4000 to c.540 million years ago, Ma), but the oceans are

21 hypothesised to have become progressively oxygen-rich during the Ediacaran-

22 Cambrian transition interval, coincident with the rise of animal life. We utilise the

23 uranium isotope ratio of seawater (²³⁸U/²³⁵U; reformulated as $\delta^{238}\text{U}$), an effective

24 tracer of oceanic redox conditions, as a proxy for changes in the global proportion of

25 anoxic seafloor. We present a new $\delta^{238}\text{U}$ dataset for carbonate rocks from the Lower

26 Nama Group, Namibia, deposited in a shelf ramp succession during the terminal

27 Neoproterozoic (~550 to ~547 Ma). These data have persistently low $\delta^{238}\text{U}$ (average

28 = $-0.81 \pm 0.06\text{‰}$) compared with the signature of modern day seawater. Such low

29 $\delta^{238}\text{U}$ are consistent with enhanced U drawdown from the water column under anoxic
30 conditions, and the preferential export of ‘heavy’ ^{238}U to sediments following U(VI)-
31 U(IV) reduction. Placing our results into a steady state ocean box model suggests at
32 least a third of the global seafloor was covered by anoxic bottom waters compared
33 with only 0.3% in today’s oxygenated oceans. Comparison with $\delta^{238}\text{U}$ from older
34 sediments deposited in other basins further supports an expansion of anoxic bottom
35 waters towards the end of the Ediacaran. Our data are consistent with an emerging
36 picture of a dominantly anoxic Ediacaran ocean punctuated by brief ocean
37 oxygenation events. In the Nama Group, the transition towards globally widespread
38 anoxic conditions post-dates the first appearance of both skeletal metazoans and soft-
39 bodied fauna of the Nama Assemblage. This suggests that the global expansion of
40 anoxia did not coincide with the decline of the Ediacaran biota, or drive the biotic
41 turnover between the White Sea and Nama Assemblages. The impact of this global
42 redox change on metazoan ecosystems is unclear, since the expansion of anoxia, if
43 contained mainly within deeper waters, may not have impinged significantly upon
44 continental shelves that host the majority of biodiversity.

45

46 **1. Introduction**

47 The oxygen-deficient Proterozoic oceans (2500 to c.540 million years ago,
48 Ma) were characterised by ferruginous (anoxic and iron rich) conditions, with
49 oxygenated surface waters and occasional euxinia (anoxia and free- H_2S) at mid-
50 depths (Poulton and Canfield, 2011). The oceans are thought to have become
51 progressively oxygenated in the Cryogenian, Ediacaran and Cambrian Periods (720 -
52 485 Ma), coincident with the rise of animal life (Canfield et al., 2007; Planavsky et
53 al., 2014; Sahoo et al., 2012). However, the overall trend towards more oxygenated

54 conditions has been difficult to constrain, because reconstructions have relied on
55 localised redox proxies that record heterogeneous oceanic conditions among
56 Neoproterozoic basins. Deepwater oxygenation has been recorded as early as 580 Ma
57 in some basins, but others remained largely anoxic into the early Phanerozoic
58 (Bowyer et al., 2017; Canfield et al., 2007; Wood et al., 2015). In particular, a recent
59 compilation of Fe-speciation data, which records regional anoxia, from sediments
60 deposited below storm wave base in multiple basins, finds no statistically significant
61 trend towards oxygenation across the Ediacaran–Cambrian transition period (Sperling
62 et al., 2015). Together, this suggests that widespread deep water oxygenation did not
63 occur until the Palaeozoic Era. However, such reconstructions based on localised
64 redox proxies have only limited potential to constrain global trends in marine redox
65 conditions due to incomplete coverage, bias in preserved facies, and hydrodynamic
66 controls on local redox conditions that do not relate to changes in atmospheric oxygen
67 levels.

68 Attempts to constrain the global extent of atmospheric and ocean oxygenation
69 commonly are based on i) constraints on the burial of organic carbon and sulfide
70 using carbon ($^{13}\text{C}/^{12}\text{C}$; $\delta^{13}\text{C}$) and sulfur isotopes ($^{34}\text{S}/^{32}\text{S}$; $\delta^{34}\text{S}$), ii) sedimentary
71 enrichments or depletions in the redox-sensitive elements (e.g. uranium, vanadium,
72 cerium, iodine and molybdenum), and iii) compositional shifts in various redox-
73 sensitive metal stable isotope systems (e.g. chromium, selenium and molybdenum).
74 However, these systems produce conflicting results for the onset of ocean
75 oxygenation, with a very broad range that spans almost 300 Myr, from ca. 800 to 520
76 Ma (Fike et al., 2006; Kendall et al., 2015; Planavsky et al., 2014; Sahoo et al., 2012;
77 Stolper and Keller, 2018). These conflicting findings may in part be due to the unique
78 reduction potential of each system, each of which would have been surpassed

79 progressively, and their different oceanic residence times which affect the timescale
80 of response. Enrichments in redox sensitive trace metals in black shales suggest that
81 rather than a single, unidirectional step change in oxygenation, the oceans instead
82 remained broadly anoxic throughout the Neoproterozoic, but hosted a series of large
83 perturbations, dubbed ‘ocean oxygenation events (OOEs)’ (Sahoo et al., 2016).

84 The timing of oceanic oxygenation is significant as it is hypothesised to have
85 coincided with the rise of macroscopic metazoan life (Canfield et al., 2007). Body
86 fossils of putative metazoans are first recorded ~571 Ma (Pu et al., 2016), but
87 burrowing animals did not appear until after 560 Ma (Budd and Jensen, 2017). The
88 earliest skeletal macrofossils appear globally ~550 Ma (Germs, 1983). The
89 development of hard body parts is energetically costly, and explanations for the
90 abrupt and globally synchronous emergence of biomineralisation have included
91 ecological factors such as a rise in predation, and environmental factors, such an
92 increase in alkalinity, or increased oxygen availability (Hua et al., 2003; Wood et al.,
93 2017). Proxies that record the global extent of anoxia are required to investigate
94 relationships between the innovation and distribution of biota, and major
95 environmental change.

96 Using techniques in multiple-collector ICP-MS (MC-ICPMS) and double-
97 spiking, we present coupled uranium isotope ($\delta^{238}\text{U}$) and U concentration
98 (approximated by U/Ca) data preserved in carbonate rocks from the lower Nama
99 Group, Namibia. Radiometric ages, as well as the presence of well-preserved biota,
100 and globally correlative carbon isotope trends provide some constraints on the timing
101 of deposition of the Nama Group (for geological and geochemical background, see
102 SI-1). The integration of local and global redox proxies, in a section that directly
103 preserves changes in biota, allows for co-interpretation without a need to correlate

104 between possibly contemporaneous sections. These new results constrain global
105 oceanic redox conditions spanning the interval from ~550--~547 Ma, and suggest
106 anoxic bottom waters expanded to cover at least a third of the sea floor, following the
107 emergence of the first skeletal animals and coincident with major perturbations in the
108 sulfur and carbon cycles (Cui et al., 2016; Fike et al., 2006; Tostevin et al., 2017;
109 Wood et al., 2015).

110

111 **1.1 The Uranium isotope paleo-redox proxy**

112 Uranium primarily enters the ocean through riverine runoff, and in the modern ocean,
113 U burial is split between sediments below anoxic bottom waters (20%), euxinic
114 sediments below productive but oxygenated waters (23%), carbonates (23%), deltaic
115 sediments (19%) and altered oceanic crust (10%)(Andersen et al., 2017; Dunk et al.,
116 2002) (Figure 1). Given that anoxic sediments account for less than 0.3% of the
117 modern seafloor (Andersen et al., 2017; Dunk et al., 2002), U removal into anoxic
118 sediments, which occurs via the reduction of highly soluble U(VI) to relatively
119 insoluble U(IV), is disproportionately high. This makes the concentration of U in
120 seawater very sensitive to the global extent of anoxia. Additionally, although the U
121 isotope proxy has so far only been calibrated in modern euxinic settings, U reduction
122 and removal should occur under all anoxic conditions. If this is the case, then U
123 isotope systematics provide information on the total anoxic water mass. This differs
124 from the isotope systematics of some other palaeo-redox proxies which instead reflect
125 the end-member redox state of anoxic and sulfidic conditions (e.g. Molybdenum).

126 In nature, the largest uranium isotope fractionations have been documented
127 during oxidation-reduction associated with the U(VI)-U(IV) exchange reaction,
128 resulting from variable nuclear volumes and electron density distributions between

129 the different U isotopes (Abe et al., 2008). During the reduction of U(VI) to U(IV)
130 under anoxic conditions, authigenic U enrichment occurs in the sediments as
131 dispersed U(IV) precipitates (e.g. uranite), leaving the anoxic water column depleted
132 in dissolved U. ^{238}U is preferentially removed into the sediments, leaving seawater
133 depleted in this heavy isotope. The magnitude of this redox-related fractionation
134 between ^{238}U and ^{235}U is at the permil-level (Stirling et al., 2007; Weyer et al., 2008),
135 and dominates the U isotope signature of seawater.

136 In the modern environment, the $\delta^{238}\text{U}$ signature in seawater is well constrained
137 ($-0.39 \pm 0.01\text{‰}$), and appears to be slightly lower than the mean signature of riverine
138 input (-0.26‰) (Andersen et al., 2017; Stirling et al., 2007; Weyer et al., 2008). This
139 is largely a result of ^{238}U - ^{235}U fractionation during U burial in anoxic settings, despite
140 these settings only accounting for a small proportion of the modern seafloor. Uranium
141 has a long residence time in the modern ocean of $\sim 400 \pm 120$ thousand years (kyr),
142 and behaves conservatively (Dunk et al., 2002). The $\delta^{238}\text{U}$ of modern seawater is
143 therefore globally homogeneous and captures changes in the strength of the anoxic
144 sink over long timescales.

145 Uranium exists in seawater predominantly as the uranyl-tricarbonate ion
146 $[\text{UO}_2(\text{CO}_3)_3]^{4-}$, and this soluble form of uranium is directly incorporated into calcium
147 carbonate. There is a growing body of evidence showing that, under most oceanic
148 conditions, modern marine carbonate sediments preserve seawater $\delta^{238}\text{U}$ signatures
149 ($\delta^{238}\text{U}_{\text{sw}}$) without large U isotope fractionations (Andersen et al., 2014; Chen et al.,
150 2018; Romaniello et al., 2013; Stirling et al., 2007; Tissot and Dauphas, 2015; Weyer
151 et al., 2008), provided minimal diagenetic exchange of the U isotopes has occurred
152 following deposition. $\delta^{238}\text{U}$ in ancient carbonate rocks has therefore been successfully

153 used as a global paleo-redox proxy (Andersen et al., 2014; Clarkson et al., 2018; Lau
154 et al., 2017, 2016; Stirling et al., 2007; Zhang et al., 2018).

155 Early diagenesis has been observed to systematically drive $\delta^{238}\text{U}$ to higher
156 values in some recent carbonates, especially those derived of primary metastable
157 aragonite or aragonite-calcite mixtures, resulting in a positive offset from modern
158 seawater of up to 0.3‰ (Romaniello et al., 2013). This offset is present in the
159 majority of Holocene aragonitic sediments from the Bahamas, even those deposited
160 below oxygenated bottom waters (Chen et al., 2018). As such, early diagenetic
161 enrichments in ^{238}U with respect to ^{235}U cannot be easily detected using redox proxies
162 such as Ce anomalies or Fe speciation (Chen et al., 2018; Hood et al., 2018). In
163 addition, fabric specific work on Cryogenian carbonates has demonstrated that early
164 cements, micrite and ooids may preserve primary $\delta^{238}\text{U}$ while microbialites and burial
165 cements generally have altered $\delta^{238}\text{U}$ (Hood et al., 2018, 2016). However, if burial
166 diagenesis is occurring under closed system conditions, the phase specific variability
167 may be averaged, meaning the bulk rock values could still provide a reliable
168 approximation of the initial primary signal.

169

170 **2. Methods**

171 The Nama Group, Namibia, is a mixed carbonate-siliciclastic sequence
172 deposited in a ramp system, and exceptional exposure has allowed sequence
173 stratigraphic, geochemical analysis and ecological surveys across multiple transects
174 (see SI-1). Samples from a range of carbonate facies were selected from the Zebra
175 River Section, which covers the Lower and Upper Omkyk, and Hoogland Members.
176 The carbonates were probably originally deposited dominantly as aragonite, but have
177 since neomorphosed to calcite. Dolomite-rich samples were excluded due to

178 uncertainty surrounding the impact of dolomitisation on $\delta^{238}\text{U}$, $\delta^{13}\text{C}$ ($^{13}\text{C}/^{12}\text{C}$;
179 reformulated as $\delta^{13}\text{C}$), $\delta^{18}\text{O}$ ($^{18}\text{O}/^{16}\text{O}$; reformulated as $\delta^{18}\text{O}$), $\delta^{34}\text{S}$ ($^{34}\text{S}/^{32}\text{S}$;
180 reformulated as $\delta^{34}\text{S}$), major element, Fe-speciation and rare earth element data for
181 the same samples, and the associated methods are published in Tostevin et al., (2017,
182 2016) and Wood et al., (2015).

183 All samples were prepared and analysed for their $\delta^{238}\text{U}$ composition at the
184 Centre for Trace Element Analysis, University of Otago, New Zealand following
185 protocols reported in SI-2. In brief, powders were subjected to a two-step reductive
186 and oxidative cleaning procedure to remove potential Mn-oxides and residual organic
187 matter (Clarkson et al., 2018). Carbonate was then selectively digested using a 1M
188 sodium acetate buffer solution maintained at $\text{pH} > 5$, which avoids attacking the
189 silicate fraction, as demonstrated by low Al concentrations (< 20 ppm) (Table S2). The
190 digest was resuspended in nitric acid and analysed via quadrupole ICP-MS to
191 determine the concentrations of trace metals, including U and Ca. Based on the U
192 concentration, leachates were subsampled to achieve a total U mass of 30-150 ng, and
193 double spiked to give a $^{236}\text{U}/^{235}\text{U}$ ratio of approximately 3. Matrix elements (e.g. Na,
194 Ca) were first removed through co-precipitation using pre-cleaned FeCl_3 and
195 ammonia solution (Clarkson et al., 2018). The resulting precipitates were first
196 dissolved in 6M HCl, and then resuspended in 3M HNO_3 and loaded onto heat shrink
197 teflon columns containing UTEVA resin. Samples were then oxidised to eliminate
198 any organic residues from the resin.

199 The purified U fractions were re-dissolved in 2% HCl and 0.01% HF, and
200 analysed via MC-ICPMS. A ^{236}U - ^{233}U double spike was used to correct for
201 instrumental mass fractionation (Rolison et al., 2017; Stirling et al., 2007). The
202 $^{238}\text{U}/^{235}\text{U}$ composition is presented in δ -notation following Eq (1):

203
$$\delta^{238}\text{U} = \left(\frac{(^{238}\text{U}/^{235}\text{U})_{\text{sample}}}{(^{238}\text{U}/^{235}\text{U})_{\text{CRM-145}}} - 1 \right) \quad (1)$$

204 where CRM-145 is the ‘zero-delta’ standard. For a detailed method description, see
205 SI-2 and references therein.

206

207 **3. Results and assessment of diagenesis**

208 U/Ca decreases up-section from scattered but generally higher values in the
209 Lower Omkyk Member (average = 0.63 ± 0.28 $\mu\text{mol/mol}$ (1 SE), range = 0.22 to 1.04
210 $\mu\text{mol/mol}$) to lower, more stable values in the Upper Omkyk and Hoogland Members
211 (average = 0.21 ± 0.09 $\mu\text{mol/mol}$ (1 SE), n=14, range = 0.11 to 0.41 $\mu\text{mol/mol}$)
212 (Figure 2, Table S2). $\delta^{238}\text{U}$ decreases systematically from a maximum of -0.27‰ in
213 the Lower Omkyk Member to a stable baseline of -0.81 ± 0.06 ‰ (1 SE) for the Upper
214 Omkyk and Hoogland Members (excluding ZR29 at 168.1 m, with an outlying $\delta^{238}\text{U}$
215 of -0.48‰). One outlying sample (LO4 at 18 m) deviates from this trend and has a
216 lower $\delta^{238}\text{U}$ than the adjacent samples of -0.97‰ (Figure 2, Table S2). For a full
217 assessment of the impacts of local water column redox conditions during deposition,
218 facies control, early and late stage diagenesis, and detrital leaching, see SI-3 and SI-4.

219 There are several compelling reasons to suggest that the $\delta^{238}\text{U}$ in the Nama
220 Group record a primary open ocean signature. Firstly, there is limited stratigraphic
221 variability in $\delta^{238}\text{U}$ for the Upper Omkyk and Hoogland Members. Secondly, the
222 rocks generally preserve primary marine geochemical signals based on other
223 diagnostic parameters, including $\delta^{13}\text{C}$ and rare earth element patterns (Tostevin et al.,
224 2016; Wood et al., 2015). Furthermore, the co-occurring $\delta^{13}\text{C}$ is relatively enriched,
225 suggesting minimal overprinting during meteoric diagenesis, and this is supported by
226 petrographic analysis (Wood et al., 2018). While these parameters cannot be relied
227 upon to identify alteration of $\delta^{238}\text{U}$, they suggest the Nama Group has the potential to

228 preserve primary marine $\delta^{238}\text{U}$ (Chen et al., 2018; Hood et al., 2018). Thirdly, these
229 samples have low TOC (<0.2 wt%) and were deposited under a locally oxygenated
230 water column, and should therefore act as a passive sink for seawater U (Wood et al.,
231 2015). Fourth, the Nama Group samples analysed here are composed of high purity
232 samples (>90% CaCO_3) that preserve textural detail (Wood et al., 2018), indicating
233 that neomorphism from primary aragonite occurred early and in the presence of fluids
234 similar in composition to seawater. Finally, and most significantly, the Nama Group
235 $\delta^{238}\text{U}$ closely matches pene-contemporaneous $\delta^{238}\text{U}$ from carbonates deposited in two
236 independent sections from a geographically distant basin in South China (Zhang et al.,
237 2018).

238 The $\delta^{238}\text{U}$ from south China display a similarly low $\delta^{238}\text{U}$ centred around -
239 $0.95 \pm 0.10\text{‰}$ and $-0.97 \pm 0.09\text{‰}$ for Gaojiashan and Wuhe sections, respectively
240 (Zhang et al., 2018), together confirming that low $\delta^{238}\text{U}$ is a primary global signal
241 from the late Ediacaran. $\delta^{238}\text{U}$ from the oldest part of the Xiaotan section, south China
242 reported in Wei et al., (2018) also capture the minima in $\delta^{238}\text{U}$ around -1‰ .
243 Additionally, the systematic trend towards lower $\delta^{238}\text{U}$ in the Lower Nama Group is
244 also captured in equivalent sections from south China (Zhang et al., 2018). Zhang et
245 al. (2018) screened their $\delta^{238}\text{U}$ data using a number of geochemical criteria, including
246 Mn/Sr ratios <2.5, although there is no evidence to suggest that Mn/Sr cut-offs can be
247 reliably used to screen for alteration of $\delta^{238}\text{U}$ in bulk carbonate rocks (Chen et al.,
248 2018). In Figure 3, we plot the un-screened $\delta^{238}\text{U}$ for comparison, and the trend from
249 near-modern $\delta^{238}\text{U}$ to very low $\delta^{238}\text{U}$ is apparent in all three sections.

250 Despite similar trends, the Nama Group does not appear to record the minima
251 in $\delta^{238}\text{U}$ observed in south China. While there are numerous lines of evidence to
252 suggest the Lower Nama Group and the Dengying Formation were deposited at

253 similar times, including capturing similar $\delta^{13}\text{C}$ and $\delta^{34}\text{S}$, the presence of the Nama
254 biota, and overlapping radiometric dates, there is some uncertainty in dating and
255 correlations that mean the sections could either be contemporaneous or very close in
256 age (Cui et al., 2016; Tostevin et al., 2017; Zhang et al., 2018). If the Nama Group
257 was deposited slightly earlier than the Dengying, it may not record the full breadth of
258 the transition to a very low $\delta^{238}\text{U}$ of around -1‰. Alternately, if the sections were
259 deposited at precisely the same time, then there may be a diagenetic offset of 0.1-
260 0.2‰ in the Nama section (see full discussion of diagenetic effects in SI-3, SI-4 and
261 Figure S1). Since diagenetic alteration in shallow modern carbonate sediments
262 generally results in higher $\delta^{238}\text{U}$ (Chen et al., 2018; Hood et al., 2018), the minimum
263 values recorded globally may be more representative of seawater signatures. This
264 suggests that the lowest $\delta^{238}\text{U}$ as recorded in south China might be closest to seawater
265 $\delta^{238}\text{U}$ for the latest Ediacaran.

266

267 **4. Discussion**

268 **4.1 Ediacaran seawater $\delta^{238}\text{U}$**

269 There are some higher $\delta^{238}\text{U}$ in the Lower Omkyk Member (up to -0.27‰)
270 which give rise to an apparent systematic, secular trend of decreasing $\delta^{238}\text{U}$ up section
271 towards a baseline of $-0.81 \pm 0.06\text{‰}$ in the Upper Omkyk and Hoogland Members.
272 This $\delta^{238}\text{U}$ baseline sits 0.43‰ below the $\delta^{238}\text{U}$ of modern seawater and may
273 represent a maximum estimate of seawater $\delta^{238}\text{U}$ at the time of deposition. If we
274 assume that the higher $\delta^{238}\text{U}$ and generally higher U/Ca represents a primary signal,
275 these trends can be interpreted to reflect the progressive removal of U from the water
276 column and preferential export of heavy ^{238}U to sediments under expanding seafloor
277 anoxia in the latest Ediacaran. Primary trends in the Lower Omkyk Member of the

278 Nama Group are supported by comparisons with the $\delta^{238}\text{U}$ of organic-rich mudrocks
279 ($\delta^{238}\text{U}_{\text{ORM}}$) from Member IV of the Doushantuo Formation, South China (Kendall et
280 al., 2015), deposited immediately before the Nama Group at 560-551 Ma. The
281 $\delta^{238}\text{U}_{\text{SW}}$ for this time period can be calculated from the $\delta^{238}\text{U}_{\text{ORM}}$, using an assumed U
282 isotope fractionation factor between seawater and the anoxic sinks of 0.6‰ (Kendall
283 et al., 2015). This gives an average $\delta^{238}\text{U}_{\text{SW}}$ of $-0.34 \pm 0.11\%$ (excluding anomalously
284 low values at the top of the cores) which is within error of the modern ocean value of
285 $-0.39 \pm 0.01\%$ (Andersen et al., 2017, 2014; Rolison et al., 2017; Tissot and Dauphas,
286 2015). This result was interpreted as indicating widespread marine oxygenation, and
287 is supported by oxygenated signals from molybdenum (Mo) isotopic signatures on the
288 same samples.

289 The decrease in average $\delta^{238}\text{U}_{\text{SW}}$ from -0.34% to -0.81% , obtained by
290 combining the average $\delta^{238}\text{U}$ during Doushantuo deposition (~ 560 to ~ 551 Ma) with
291 the average $\delta^{238}\text{U}$ during Nama Group deposition (~ 550 to ~ 547 Ma), implies
292 increased U(IV) removal from seawater and the preferential export of heavy ^{238}U
293 from the water column around 550 Ma (Figure 1 and 4). Lower $\delta^{238}\text{U}_{\text{ORM}}$ of -1.02%
294 observed in the youngest rocks of the Doushantuo cores (Kendall et al., 2015) could
295 indicate the onset of this anoxia expansion, and be equivalent to the apparent secular
296 trends seen in the lower Nama Group and Dengying Formation (Zhang et al., 2018).
297 Further, U/TOC in Member IV of the Doushantuo Formation supports declining U
298 concentrations ~ 550 Ma (Sahoo et al., 2016), consistent with declining average U/Ca
299 across the Lower Nama Group, suggesting U drawdown under expanded ocean
300 anoxia. Overall, the trends in $\delta^{238}\text{U}$ and U/Ca in the Nama Group, when compared
301 with $\delta^{238}\text{U}$ from the Doushantuo Formation and the Dengying Formation, fit well with

302 global trends and support a rapid and dramatic decrease in $\delta^{238}\text{U}$ around 550 Ma
303 (Figure 4).

304

305 **4.2 Constraining the extent of anoxia during the Ediacaran**

306 Low $\delta^{238}\text{U}_{\text{SW}}$ is broadly consistent with an expansion of seafloor anoxia, and
307 we use an ocean box model to explore the implications of a $\delta^{238}\text{U}_{\text{SW}}$ of -0.81‰ for the
308 Ediacaran ocean redox state after Zhang et al., (2018b), as follows:

$$309 \quad \delta^{238}\text{U}_{\text{SW}} = \frac{[\delta^{238}\text{U}_{\text{riv}} - (A_{\text{anox}}*k_{\text{anox}}*\Delta_{\text{anox}}) + (A_{\text{low}}*k_{\text{low}}*\Delta_{\text{low}}) + (A_{\text{oxic}}*k_{\text{oxic}}*\Delta_{\text{oxic}})]}{(A_{\text{anoxic}}*k_{\text{anoxic}}) + (A_{\text{low}}*k_{\text{low}}) + (A_{\text{oxic}}*k_{\text{oxic}})} \quad (1)$$

310 For a full description of the model structure and derivation of equation 1, see SI-5. In
311 equation 1, $\delta^{238}\text{U}_{\text{riv}}$ is the modern riverine $\delta^{238}\text{U}$, prescribed here as $\delta^{238}\text{U}_{\text{riv}} = -0.30\text{‰}$,
312 consistent with previous models and the average for upper continental crust ($-0.29 \pm$
313 0.06‰) (Andersen et al., 2017; Montoya-Pino et al., 2010; Zhang et al., 2018).

314 Variable k is the effective burial rate constant for each of the three burial sinks, and is
315 derived by inverting the area and burial fluxes of U in modern environments (Zhang
316 et al., 2018). The model assumes that uranium enters the ocean through rivers, and
317 leaves via three major sinks: sediments below anoxic, low oxygen or oxic bottom
318 waters. Here, low oxygen is defined as deposition below bottom waters containing 0.2
319 - 2 ml/L of dissolved O_2 and the anoxic sink includes deposition below both anoxic
320 ferruginous and euxinic waters. The oxic sink is an amalgamation of several minor
321 sinks, including Fe-Mn crusts, carbonate sediments, pelagic clays, alteration of oceanic
322 crust, and coastal retention. The U isotope fractionation associated with the oxic and
323 low oxygen sinks is small (0.005‰ and 0.1‰ respectively; Andersen et al., 2017).

324 We take the U isotope fractionation factor between seawater and anoxic sinks, Δ_{anox} ,
325 to be 0.6‰ (Andersen et al., 2014; Rolison et al., 2017). The area of anoxic, low
326 oxygen and oxic seafloor (A_{anox} , A_{low} and A_{oxic}) is determined by the total area of

327 seafloor ($A_{\text{ocean}}=3.61*10^{16} \text{ dm}^2$) multiplied by the fraction of seafloor covered by
328 anoxic (F_{anox}), low oxygen (F_{low}) or oxic (F_{ox}) bottom waters, respectively. F_{anox} is
329 allowed to vary between 0 and 1. F_{low} covaries with F_{ox} and is assumed to remain 6%
330 of the size of the oxic sink, consistent with modern environments.

331 Expanding ocean anoxia drives $\delta^{238}\text{U}_{\text{SW}}$ lower. To generate a $\delta^{238}\text{U}_{\text{SW}}$ of -
332 0.81‰ requires a large area of seafloor anoxia of 33%. The model is very insensitive
333 at low $\delta^{238}\text{U}_{\text{SW}}$, such that a large change in seafloor anoxia is required to drive a small
334 change in the resulting U isotope value (Lau et al., 2017). This means that the small
335 variations in $\delta^{238}\text{U}_{\text{SW}}$ through the section, and uncertainty about the extent of
336 diagenetic enrichment, have large implications for the calculated area of anoxic
337 seafloor. Given diagenetic enrichments may have skewed the Nama Group to higher
338 $\delta^{238}\text{U}$, 33% represents a minimum estimate of seafloor anoxia. Under the conditions
339 described above, the model cannot reproduce the very low $\delta^{238}\text{U}$ of -0.97‰ recorded
340 in south China. However, the model is sensitive to the U isotope fractionation factor
341 associated with the anoxic sink, the assumed k function, and, to a lesser extent, the
342 $\delta^{238}\text{U}$ of riverine input. We explore the sensitivity of our model to these parameters
343 below.

344 The $\delta^{238}\text{U}$ of modern rivers varies widely, depending on the geology of the
345 catchment area, since evaporites, limestones, dolomites, granites and black shales all
346 have unique $\delta^{238}\text{U}$ (Andersen et al., 2017; Stirling et al., 2007; Tissot and Dauphas,
347 2015). However, a weighted mean of all surveyed rivers gives a $\delta^{238}\text{U}_{\text{riv}}$ of -0.34‰,
348 but this average is strongly influenced by one exceptionally low $\delta^{238}\text{U}$ reported from
349 the Yangtze river (-0.70‰). If this river is excluded from the calculation, the global
350 mean riverine $\delta^{238}\text{U}$ is -0.26‰ (Andersen et al., 2017). In general, lower $\delta^{238}\text{U}_{\text{riv}}$
351 results in a smaller estimate of the area of anoxic seafloor. For example, for a higher

352 $\delta^{238}\text{U}_{\text{riv}}$ of -0.26‰ a larger expanse of anoxic seafloor is required to explain the Nama
353 Group data (55%). Conversely, for a $\delta^{238}\text{U}_{\text{riv}}$ of -0.34‰, a reduced extent of anoxic
354 seafloor is implied (24%). Changes in $\delta^{238}\text{U}_{\text{riv}}$ within this range can not drive $\delta^{238}\text{U}_{\text{SW}}$
355 to the low values recorded in south China (-0.97‰), even with 100% sea floor anoxia
356 (Figure 5a).

357 Of all the fractionations involved in the U isotope system, those associated
358 with the anoxic sink are the largest but remain under constrained. Our model is highly
359 sensitive to the assumed fractionation factor, with a smaller Δ_{anox} implying a greater
360 extent of anoxia for a given $\delta^{238}\text{U}_{\text{SW}}$. We test the sensitivity of our model to extreme
361 high and low fractionation factors between 0.5 and 1.2‰ (Figure 5b). For example, a
362 larger Δ_{anox} , of 0.7‰, can be reconciled with our data with 18% of the seafloor
363 covered by anoxic bottom waters, whereas a smaller Δ_{anox} , of 0.5 cannot be reconciled
364 with our data, even if 100% of the seafloor is anoxic (Figure 5). For a $\delta^{238}\text{U}_{\text{riv}}$ of -
365 0.30‰, a minimum Δ_{anox} of 0.67‰ is required to produce a $\delta^{238}\text{U}_{\text{SW}}$ of -0.97‰, as
366 recorded in south China (Zhang et al., 2018). The model is extremely sensitive to the
367 assigned global average k_{anox} and Δ_{anox} , but both of these values are based on fluxes in
368 isolated modern anoxic water bodies such as the Black Sea and the Cariaco Basin. It
369 is not clear whether these values can be extrapolated to the past global ocean with
370 very high A_{anox} . Further U isotope studies of modern anoxic and euxinic basins are
371 required to continue to refine the magnitude of k_{anox} and Δ_{anox} , particularly under the
372 anoxic ferruginous conditions that may have typified Ediacaran oceans (Rolison et al.,
373 2017).

374 Regardless of the sensitivity of the model to various poorly constrained fluxes
375 and $\delta^{238}\text{U}$, our data cannot be explained simply by variation in the riverine
376 composition or the U isotope fractionation factor between anoxic sediments and

377 seawater (Δ_{anox}). Importantly, only changing the size of the anoxic sink is able to drive
 378 the $\delta^{238}\text{U}_{\text{sw}}$ to the very negative values observed in the Nama group, although
 379 uncertainties in riverine $\delta^{238}\text{U}$ and Δ_{anox} will impact the scale of anoxic expansion
 380 required to explain the data. The only way to reconcile our U isotope data with those
 381 from 560-550 Ma is a dramatic expansion of marine anoxia from near-modern levels
 382 to between 24% and 100% of the seafloor.

383

384 **Table 1: Parameters, symbols and selected values used in the steady state model.**

385 **Values in brackets are the ranges considered in sensitivity tests.**

Parameter	Symbol	Value	Reference
$\delta^{238}\text{U}$ of global riverine input	$\delta^{238}\text{U}_{\text{riv}}$	-0.30‰ (-0.34 to -0.26‰)	Andersen et al., 2017
$\delta^{238}\text{U}$ of Ediacaran seawater	$\delta^{238}\text{U}_{\text{SW}}$	-0.81‰ to 0.89‰	
Isotope fractionation between seawater and oxic sinks	Δ_{oxic}	0.005‰	Weyer et al., 2008
Isotope fractionation between seawater and low oxygen sinks	Δ_{low}	0.1‰	Tissot and Dauphas, 2015
Isotope fractionation between seawater and anoxic sinks	Δ_{anox}	0.6‰ (0.5-1.2‰)	Andersen et al., 2017; Weyer et al., 2008
Fraction of seafloor overlain by oxic bottom waters	F_{oxic}	$= 1 - F_{\text{low}} - F_{\text{anox}}$	
Fraction of seafloor overlain by low oxygen bottom waters	F_{low}	0.06 until $F_{\text{anox}} > 0.94$, then $F_{\text{oxic}} = 0$ and $F_{\text{low}} = 1 - F_{\text{anox}}$	
Fraction of seafloor overlain by anoxic bottom waters	F_{anox}	0 – 1	
Total area of ocean floor	A_{ocean}	3.61E16 dm ²	
Effective burial rate constant for oxic sinks	k_{oxic}	0.0536 dm/yr	Dunk et al., 2002
Effective burial rate constant for low oxygen sinks	k_{low}	0.469 dm/yr	Dunk et al., 2002
Effective burial rate constant for anoxic sinks	k_{anox}	0.939 dm/yr	Zhang et al., 2018b

386

387 **4.3 Neoproterozoic redox conditions**

388 The new $\delta^{238}\text{U}$ and U/Ca records presented here, considered in a global
389 context, suggest that there was a rapid and dramatic increase in the extent of seafloor
390 anoxia around 550 Ma (Kendall et al., 2015; Wei et al., 2018; Zhang et al., 2018)
391 (Figure 4 and 5). This transition coincides with a small positive carbon isotope
392 excursion (Figure 3, Cui et al., 2016; Zhang et al., 2018b), indicating enhanced carbon
393 burial under anoxic conditions. A shift in the marine sulfur cycle, recorded by $\delta^{34}\text{S}$,
394 occurs around the same time, possibly consistent with more widespread sulfate
395 reduction under anoxic conditions (Cui et al., 2016; Fike et al., 2006; Tostevin et al.,
396 2017). Certainly, U reduction mediated by sulfate-reducing bacteria under anoxic
397 conditions is known to drive U isotope fractionation of the direction and magnitude
398 captured by the Nama Group (Andersen et al., 2017; Stirling et al., 2015; Stylo et al.,
399 2015). One possibility is that the combined $\delta^{238}\text{U}$ and $\delta^{34}\text{S}$ data capture an intriguing
400 link between the sulfur and uranium cycles, reflecting increased euxinia in the latest
401 Ediacaran. The transition to higher $\delta^{34}\text{S}$ may additionally reflect an elevated riverine
402 flux or changing riverine source, suggesting a link between changes in weathering
403 regimes and the type and extent of anoxia (Cui et al., 2016).

404 Widespread anoxia within ten million years of the Ediacaran-Cambrian
405 boundary is consistent with recent compilations of Fe-speciation data which show no
406 overall trend towards oxygenation in the Neoproterozoic (Sperling et al., 2015);
407 $\text{Fe}^{3+}/\Sigma\text{Fe}$ ratios in submarine basalts which place deep ocean oxygenation in the Late
408 Palaeozoic (Stolper and Keller, 2018); biogeochemical models which predict a rise in
409 oxygen around 400 Ma (Bergman et al., 2004), as well as molybdenum isotope data
410 which place the oxygenation of the oceans in the Palaeozoic (~520 to 400 Ma) (Chen
411 et al., 2015). In addition, earlier work based on Th/U ratios suggests the

412 Precambrian-Cambrian Boundary was associated with the widespread development of
413 anoxic shallow marine environments (Kimura and Watanabe, 2001). Together, this
414 evidence suggests that there was no unidirectional change in marine oxygenation
415 during the Neoproterozoic, and instead that the oceans remained broadly anoxic until
416 later in Earth's history. Although the relationship between local and global oceanic
417 redox conditions is complex, local redox proxy data are consistent with
418 heterogeneous, poorly ventilated basins at ~550 Ma (Bowyer et al., 2017; Sperling et
419 al., 2015; Wood et al., 2015).

420 Sahoo et al., (2016) proposed a series of ocean oxygenation events (OOEs)
421 within the broadly anoxic Neoproterozoic ocean. A compilation of $\delta^{238}\text{U}_{\text{SW}}$ across the
422 Neoproterozoic and early Palaeozoic (Figure 4) reveals dramatic oscillations that
423 coincide with proposed OOEs. Our data could capture the end of OOE 3, ~560 Ma,
424 and the transition back to widespread anoxia (Figure 4). $\delta^{238}\text{U}$ data from the Yanjiahe
425 Formation and Zhujiayang Formation in south china highlight another oxygenation
426 event (OOE 4), at the base of the Cambrian, followed by a slow return to global
427 anoxia (Wei et al., 2018). Similarly, $\delta^{238}\text{U}$ data as well as trace metal enrichments
428 record a brief oxygenation event after the Sturtian glaciation (650 – 630 Ma),
429 followed by a return to anoxic conditions (Lau et al., 2017; Sahoo et al., 2012; Figure
430 4). It appears that oceanic redox conditions oscillated dramatically several times
431 before any permanent switch to a new stable oxygenated state occurred, but the driver
432 for such rapid and global change remains enigmatic. One possibility is that step
433 changes in the burial of phosphorus and organic carbon, driven by evolutionary
434 innovations, progressively lowered marine phosphate levels. Each step change would
435 result in a pulse of marine oxygenation, but over long timescales the decrease in
436 $\text{C}_{\text{org}}/\text{P}$ burial ratios would drive atmospheric oxygen levels down, and slowly

437 deoxygenate the oceans (Lenton and Daines, 2018). One possible evolutionary driver
438 is the onset of increasingly complex bioturbation during the late Ediacaran and
439 Cambrian. Fine meiofaunal traces, capable of disrupting the sediment-mat interface,
440 appeared after 560 Ma, coincident with OOE 3 (Budd and Jensen, 2017; Lenton and
441 Daines, 2018). The onset of more complex forms of burrowing, including shallow
442 penetrative burrows, appears close to the Cambrian Boundary, and could be the driver
443 for OOE 4 (Jensen et al., 2000).

444

445 **4.4 Implications for early animal ecosystems**

446 Widespread anoxia may present both a challenge and an opportunity for
447 marine ecosystems (Wood and Erwin, 2017). Anoxia can drive mass extinctions,
448 through habitat loss or contraction as well as indirect effects on nutrient availability
449 (Hull et al., 2015). But by removing incumbents, mass extinction events disrupt
450 established ecological niches, leaving them open for new taxa to colonise (Hull et al.,
451 2015). There is evidence around 550 Ma for a biotic turnover and reduction in
452 diversity between the soft bodied macrobiotas known as the White Sea and Nama
453 Assemblages (Waggoner, 2003). The Nama Assemblage, however, also marks a
454 diversification of bilaterian trace fossils (Tarhan et al., 2018), and the emergence of
455 new innovations including metazoan biomineralization (Germs, 1983). A global
456 expansion of anoxia has been proposed to coincide with decline of the Ediacaran
457 biota around 550 Ma (Zhang et al., 2018).

458 The Nama Group is relatively well dated radiometrically and hosts skeletal as
459 well as soft-bodied biota from the Nama Assemblage. Our integrated data
460 demonstrate that the transition towards globally widespread anoxic conditions post-
461 dates both the first appearance of the Nama Assemblage, and skeletal metazoans.

462 Soft-bodied biota belonging to the Nama Assemblage are recorded in the Kanies
463 Member (Bowyer et al., 2017), which sits stratigraphically below the lower Omkyk
464 Member so pre-dating the $\delta^{238}\text{U}$ transition to expanded anoxia. Skeletal *Cloudina* is
465 present in the Mara Member (Germs, 1983), which was deposited coincident with the
466 Kanies Member and the lower part of the Lower Omkyk Member, and so predates the
467 $\delta^{238}\text{U}$ minima. These data show that the global expansion of anoxia cannot have
468 driven the decline in the Ediacaran biota or biotic turnover. They may, instead, reflect
469 a geochemical response to ecological change (Lenton and Daines, 2018).

470 Following the global expansion of anoxia, our model suggests that more than a
471 third of the sea floor was covered by anoxic bottom waters. However, there is no
472 evidence that this transition impacted on the diversity or distribution of biota within
473 the Nama Group (Bowyer et al., 2017). Expanded anoxia does not necessarily have to
474 restrict shallow habitable space, if the oxygen minimum zone expands downwards
475 into deeper waters. Modern continental shelf settings (defined as shallower than 150
476 m) make up less than 10% of the modern sea floor, and yet host the majority of
477 benthic biodiversity. The abyssal plain, in contrast, comprises over 70% of the sea
478 floor. The Nama Group records a continental shelf ramp system with no basinal
479 facies, so it is possible that a global expansion of seafloor anoxia, if contained within
480 deeper waters, did not impinge on shallow shelf communities. The Nama Group,
481 therefore, demonstrates that complex metazoan communities can thrive in locally
482 well-oxygenated niches despite globally widespread anoxia (Tostevin et al., 2016;
483 Wood et al., 2015).

484

485 **5. Conclusions**

486 We present a new $\delta^{238}\text{U}$ dataset from carbonate rocks from the Nama Group,
487 Namibia, deposited at ~550-547 Ma. We report a transition from a U isotope
488 signature equivalent to the modern marine $\delta^{238}\text{U}$, to much lower $\delta^{238}\text{U}$, reaching an
489 average of $-0.81 \pm 0.06\%$. Correlations between $\delta^{238}\text{U}$ and other global sections
490 indicate this average could represent a maximum estimate of $\delta^{238}\text{U}_{\text{sw}}$. Comparison
491 with $\delta^{238}\text{U}$ observations from black shales in directly underlying strata from south
492 China further supports a dramatic shift in $\delta^{238}\text{U}_{\text{sw}}$ around ~550 Ma. We use a mass
493 balance model to explore the implications of this $\delta^{238}\text{U}$ transition, and find that
494 oceanic conditions must have switched from broadly oxygenated (with <0.3% of the
495 seafloor covered by anoxic bottom waters) to having widespread anoxic bottom
496 waters (at least a third of the seafloor). Integrated geochemical and biotic records
497 reveal that the redox transition post-dates the first appearance of skeletal fauna and
498 soft-bodied biota belonging to the Nama Assemblage. These data conclusively
499 demonstrate that expanded anoxia cannot have driven the biotic turnover between the
500 White Sea and Nama Assemblages, and may instead be a response to ecological
501 change.

502 **Acknowledgements**

503 We thank Chris Reinhard, one anonymous reviewer and editor Lou Derry for their
504 detailed and thoughtful suggestions. R.T., M.O.C., S.G. and C.H.S., were supported
505 by the Royal Society of New Zealand, Marsden Fund Standard Grant UOO1314. RT,
506 GAS and RAW acknowledge financial support from NERC's Life and the Planet
507 project (NE/1005978/1). We are grateful to L. and G. Fourie for access to Zebra River
508 farm, and Gerd Winterleitner for help with field work. Thank you to David Barr and
509 Malcolm Reid for support in the lab.

510

511 **Author contributions**

512 RT, FB, AMP and RW collected the samples. RT prepared the samples with
513 assistance from MOC, SG and CHS. RT created the model with MOC. RT interpreted
514 the data and drafted the manuscript with input from all co-authors.

515

516 **References**

- 517 Abe, M., Suzuki, T., Fujii, Y., Hada, M., Hirao, K., 2008. An ab initio molecular
518 orbital study of the nuclear volume effects in uranium isotope
519 fractionations. *J. Chem. Phys.* 129, 164309.
520 <https://doi.org/10.1063/1.2992616>
- 521 Andersen, M.B., Romaniello, S., Vance, D., Little, S.H., Herdman, R., Lyons, T.W.,
522 2014. A modern framework for the interpretation of ²³⁸U/²³⁵U in
523 studies of ancient ocean redox. *Earth Planet. Sci. Lett.* 400, 184–194.
524 <https://doi.org/10.1016/j.epsl.2014.05.051>
- 525 Andersen, M.B., Stirling, C.H., Weyer, S., 2017. Uranium Isotope Fractionation.
526 *Rev. Mineral. Geochem.* 82, 799–850.
527 <https://doi.org/10.2138/rmg.2017.82.19>
- 528 Bergman, N.M., Lenton, T.M., Watson, A.J., 2004. COPSE: a new model of
529 biogeochemical cycling over Phanerozoic time. *Am. J. Sci.* 304, 397–437.
- 530 Bowyer, F., Wood, R.A., Poulton, S.W., 2017. Controls on the evolution of
531 Ediacaran metazoan ecosystems: A redox perspective. *Geobiology* 15,
532 516–551. <https://doi.org/10.1111/gbi.12232>
- 533 Budd, G.E., Jensen, S., 2017. The origin of the animals and a 'Savannah' hypothesis
534 for early bilaterian evolution. *Biol. Rev.* 92, 446–473.
535 <https://doi.org/10.1111/brv.12239>

536 Canfield, D.E., Poulton, S.W., Narbonne, G.M., 2007. Late-Neoproterozoic Deep-
537 Ocean Oxygenation and the Rise of Animal Life. *Science* 315, 92–95.
538 <https://doi.org/10.1126/science.1135013>

539 Chen, X., Ling, H.-F., Vance, D., Shields-Zhou, G.A., Zhu, M., Poulton, S.W., Och, L.M.,
540 Jiang, S.-Y., Li, D., Cremonese, L., Archer, C., 2015. Rise to modern levels of
541 ocean oxygenation coincided with the Cambrian radiation of animals. *Nat.*
542 *Commun.* 6. <https://doi.org/10.1038/ncomms8142>

543 Chen, X., Romaniello, S.J., Herrmann, A.D., Hardisty, D., Gill, B.C., Anbar, A.D., 2018.
544 Diagenetic effects on uranium isotope fractionation in carbonate
545 sediments from the Bahamas. *Geochim. Cosmochim. Acta* 237, 294–311.
546 <https://doi.org/10.1016/j.gca.2018.06.026>

547 Clarkson, M.O., Stirling, C.H., Jenkyns, H.C., Dickson, A.J., Porcelli, D., Moy, C.M.,
548 Strandmann, P.A.E.P. von, Cooke, I.R., Lenton, T.M., 2018. Uranium isotope
549 evidence for two episodes of deoxygenation during Oceanic Anoxic Event
550 2. *Proc. Natl. Acad. Sci.* 201715278.
551 <https://doi.org/10.1073/pnas.1715278115>

552 Cui, H., Kaufman, A.J., Xiao, S., Peek, S., Cao, H., Min, X., Cai, Y., Siegel, Z., Liu, X.-M.,
553 Peng, Y., Schiffbauer, J.D., Martin, A.J., 2016. Environmental context for the
554 terminal Ediacaran biomineralization of animals. *Geobiology*.
555 <https://doi.org/10.1111/gbi.12178>

556 Dahl, T.W., Boyle, R.A., Canfield, D.E., Connelly, J.N., Gill, B.C., Lenton, T.M.,
557 Bizzarro, M., 2014. Uranium isotopes distinguish two geochemically
558 distinct stages during the later Cambrian SPICE event. *Earth Planet. Sci.*
559 *Lett.* 401, 313–326. <https://doi.org/10.1016/j.epsl.2014.05.043>

560 Dunk, R.M., Mills, R.A., Jenkins, W.J., 2002. A reevaluation of the oceanic uranium
561 budget for the Holocene. *Chem. Geol., Geochemistry of Crustal Fluids-*
562 *Fluids in the Crust and Chemical Fluxes at the Earth's Surface* 190, 45–67.
563 [https://doi.org/10.1016/S0009-2541\(02\)00110-9](https://doi.org/10.1016/S0009-2541(02)00110-9)

564 Fike, D.A., Grotzinger, J.P., Pratt, L.M., Summons, R.E., 2006. Oxidation of the
565 Ediacaran Ocean. *Nature* 444, 744–747.
566 <https://doi.org/10.1038/nature05345>

567 Germs, G.J.B., 1983. Implications of a sedimentary facies and depositional
568 environmental analysis of the Nama group in South West Africa/Namibia.
569 *Geol. Soc. South Afr.* 11, 89–114.

570 Hood, A. v. S., Planavsky, N.J., Wallace, M.W., Wang, X., 2018. The effects of
571 diagenesis on geochemical paleoredox proxies in sedimentary carbonates.
572 *Geochim. Cosmochim. Acta* 232, 265–287.
573 <https://doi.org/10.1016/j.gca.2018.04.022>

574 Hood, A. v. S., Planavsky, N.J., Wallace, M.W., Wang, X., Bellefroid, E.J., Gueguen, B.,
575 Cole, D.B., 2016. Integrated geochemical-petrographic insights from
576 component-selective $\delta^{238}\text{U}$ of Cryogenian marine carbonates. *Geology*
577 44, 935–938.

578 Hua, H., Pratt, B.R., Zhang, L.-Y., 2003. Borings in Cloudina Shells: Complex
579 Predator-Prey Dynamics in the Terminal Neoproterozoic. *PALAIOS* 18,
580 454–459. [https://doi.org/10.1669/0883-1351\(2003\)018](https://doi.org/10.1669/0883-1351(2003)018)

581 Hull, P.M., Darroch, S.A.F., Erwin, D.H., 2015. Rarity in mass extinctions and the
582 future of ecosystems. *Nature* 528, 345–351.
583 <https://doi.org/10.1038/nature16160>

584 Jensen, S., Saylor, B.Z., Gehling, J.G., Germs, G.J.B., 2000. Complex trace fossils
585 from the terminal Proterozoic of Namibia. *Geology* 28, 143–146.

586 Kendall, B., Komiya, T., Lyons, T.W., Bates, S.M., Gordon, G.W., Romaniello, S.J.,
587 Jiang, G., Creaser, R.A., Xiao, S., McFadden, K., Sawaki, Y., Tahata, M., Shu,
588 D., Han, J., Li, Y., Chu, X., Anbar, A.D., 2015. Uranium and molybdenum
589 isotope evidence for an episode of widespread ocean oxygenation during
590 the late Ediacaran Period. *Geochim. Cosmochim. Acta* 156, 173–193.
591 <https://doi.org/10.1016/j.gca.2015.02.025>

592 Kimura, H., Watanabe, Y., 2001. Oceanic anoxia at the Precambrian-Cambrian
593 boundary. *Geology* 29, 995–998.

594 Lau, K.V., Macdonald, F.A., Maher, K., Payne, J.L., 2017. Uranium isotope evidence
595 for temporary ocean oxygenation in the aftermath of the Sturtian
596 Snowball Earth. *Earth Planet. Sci. Lett.* 458, 282–292.

597 Lau, K.V., Maher, K., Altiner, D., Kelley, B.M., Kump, L.R., Lehrmann, D.J., Silva-
598 Tamayo, J.C., Weaver, K.L., Yu, M., Payne, J.L., 2016. Marine anoxia and
599 delayed Earth system recovery after the end-Permian extinction. *Proc.*
600 *Natl. Acad. Sci.* 113, 2360–2365.

601 Lenton, T.M., Daines, S.J., 2018. The effects of marine eukaryote evolution on
602 phosphorus, carbon and oxygen cycling across the Proterozoic–
603 Phanerozoic transition. *Emerg. Top. Life Sci.* ETL20170156.
604 <https://doi.org/10.1042/ETLS20170156>

605 Montoya-Pino, C., Weyer, S., Anbar, A.D., Pross, J., Oschmann, W., Schootbrugge, B.
606 van de, Arz, H.W., 2010. Global enhancement of ocean anoxia during
607 Oceanic Anoxic Event 2: A quantitative approach using U isotopes.
608 *Geology* 38, 315–318. <https://doi.org/10.1130/G30652.1>

609 Planavsky, N.J., Reinhard, C.T., Wang, X., Thomson, D., McGoldrick, P., Rainbird,
610 R.H., Johnson, T., Fischer, W.W., Lyons, T.W., 2014. Low Mid-Proterozoic
611 atmospheric oxygen levels and the delayed rise of animals. *Science* 346,
612 635–638.

613 Poulton, S.W., Canfield, D.E., 2011. Ferruginous Conditions: A Dominant Feature
614 of the Ocean through Earth’s History. *Elements* 7, 107–112.
615 <https://doi.org/10.2113/gselements.7.2.107>

616 Pu, J.P., Bowring, S.A., Ramezani, J., Myrow, P., Raub, T.D., Landing, E., Mills, A.,
617 Hodgin, E., Macdonald, F.A., 2016. Dodging snowballs: Geochronology of
618 the Gaskiers glaciation and the first appearance of the Ediacaran biota.
619 *Geology* 44, 955–958. <https://doi.org/10.1130/G38284.1>

620 Rolison, J.M., Stirling, C.H., Middag, R., Rijkenberg, M.J.A., 2017. Uranium stable
621 isotope fractionation in the Black Sea: Modern calibration of the
622 $^{238}\text{U}/^{235}\text{U}$ paleo-redox proxy. *Geochim. Cosmochim. Acta* 203, 69–88.
623 <https://doi.org/10.1016/j.gca.2016.12.014>

624 Romaniello, S.J., Herrmann, A.D., Anbar, A.D., 2013. Uranium concentrations and
625 $^{238}\text{U}/^{235}\text{U}$ isotope ratios in modern carbonates from the Bahamas:
626 Assessing a novel paleoredox proxy. *Chem. Geol.* 362, 305–316.
627 <https://doi.org/10.1016/j.chemgeo.2013.10.002>

628 Sahoo, S.K., Planavsky, N.J., Jiang, G., Kendall, B., Owens, J.D., Wang, X., Shi, X.,
629 Anbar, A.D., Lyons, T.W., 2016. Oceanic oxygenation events in the anoxic
630 Ediacaran ocean. *Geobiology* 14, 457–468.
631 <https://doi.org/10.1111/gbi.12182>

632 Sahoo, S.K., Planavsky, N.J., Kendall, B., Wang, X., Shi, X., Scott, C., Anbar, A.D.,
633 Lyons, T.W., Jiang, G., 2012. Ocean oxygenation in the wake of the
634 Marinoan glaciation. *Nature* 489, 546–549.
635 <https://doi.org/10.1038/nature11445>

636 Sperling, E.A., Wolock, C.J., Morgan, A.S., Gill, B.C., Kunzmann, M., Halverson, G.P.,
637 Macdonald, F.A., Knoll, A.H., Johnston, D.T., 2015. Statistical analysis of
638 iron geochemical data suggests limited late Proterozoic oxygenation.
639 *Nature* 523, 451–454. <https://doi.org/10.1038/nature14589>

640 Stirling, C.H., Andersen, M.B., Potter, E.-K., Halliday, A.N., 2007. Low-temperature
641 isotopic fractionation of uranium. *Earth Planet. Sci. Lett.* 264, 208–225.
642 <https://doi.org/10.1016/j.epsl.2007.09.019>

643 Stirling, C.H., Andersen, M.B., Warthmann, R., Halliday, A.N., 2015. Isotope
644 fractionation of ²³⁸U and ²³⁵U during biologically-mediated uranium
645 reduction. *Geochim. Cosmochim. Acta* 163, 200–218.
646 <https://doi.org/10.1016/j.gca.2015.03.017>

647 Stolper, D.A., Keller, C.B., 2018. A record of deep-ocean dissolved O₂ from the
648 oxidation state of iron in submarine basalts. *Nature* 553, 323.
649 <https://doi.org/10.1038/nature25009>

650 Stylo, M., Neubert, N., Wang, Y., Monga, N., Romaniello, S.J., Weyer, S., Bernier-
651 Latmani, R., 2015. Uranium isotopes fingerprint biotic reduction. *Proc.*
652 *Natl. Acad. Sci.* 112, 5619–5624.
653 <https://doi.org/10.1073/pnas.1421841112>

654 Tarhan, L.G., Droser, M.L., Cole, D.B., Gehling, J.G., 2018. Ecological Expansion and
655 Extinction in the Late Ediacaran: Weighing the Evidence for
656 Environmental and Biotic Drivers. *Integr. Comp. Biol.* 58, 688–702.
657 <https://doi.org/10.1093/icb/icy020>

658 Tissot, F.L.H., Dauphas, N., 2015. Uranium isotopic compositions of the crust and
659 ocean: Age corrections, U budget and global extent of modern anoxia.
660 *Geochim. Cosmochim. Acta* 167, 113–143.
661 <https://doi.org/10.1016/j.gca.2015.06.034>

662 Tostevin, R., He, T., Turchyn, A.V., Wood, R.A., Penny, A.M., Bowyer, F., Antler, G.,
663 Shields, G.A., 2017. Constraints on the late Ediacaran sulfur cycle from
664 carbonate associated sulfate. *Precambrian Res.* 290, 113–125.
665 <https://doi.org/10.1016/j.precamres.2017.01.004>

666 Tostevin, R., Wood, R.A., Shields, G.A., Poulton, S.W., Guilbaud, R., Bowyer, F.,
667 Penny, A.M., He, T., Curtis, A., Hoffmann, K.H., Clarkson, M.O., 2016. Low-
668 oxygen waters limited habitable space for early animals. *Nat. Commun.* 7.
669 <https://doi.org/10.1038/ncomms12818>

670 Waggoner, B., 2003. The Ediacaran Biotas in Space and Time. *Integr. Comp. Biol.*
671 43, 104–113. <https://doi.org/10.1093/icb/43.1.104>

672 Wei, G.-Y., Planavsky, N.J., Tarhan, L.G., Chen, X., Wei, W., Li, D., Ling, H.-F., 2018.
673 Marine redox fluctuation as a potential trigger for the Cambrian
674 explosion. *Geology* 46, 587–590. <https://doi.org/10.1130/G40150.1>

675 Weyer, S., Anbar, A.D., Gerdes, A., Gordon, G.W., Algeo, T.J., Boyle, E.A., 2008.
676 Natural fractionation of ²³⁸U/²³⁵U. *Geochim. Cosmochim. Acta* 72, 345–
677 359. <https://doi.org/10.1016/j.gca.2007.11.012>

678 Wood, R., Bowyer, F., Penny, A., Poulton, S.W., 2018. Did anoxia terminate
679 Ediacaran benthic communities? Evidence from early diagenesis.

680 Precambrian Res. 313, 134–147.
681 <https://doi.org/10.1016/j.precamres.2018.05.011>
682 Wood, R., Erwin, D.H., 2017. Innovation not recovery: dynamic redox promotes
683 metazoan radiations. *Biol. Rev.* <https://doi.org/10.1111/brv.12375>
684 Wood, R., Ivantsov, A.Y., Zhuravlev, A.Y., 2017. First macrobiota
685 biomineralization was environmentally triggered. *Proc R Soc B* 284,
686 20170059. <https://doi.org/10.1098/rspb.2017.0059>
687 Wood, R.A., Poulton, S.W., Prave, A.R., Hoffmann, K.-H., Clarkson, M.O., Guilbaud,
688 R., Lyne, J.W., Tostevin, R., Bowyer, F., Penny, A.M., Curtis, A., Kasemann,
689 S.A., 2015. Dynamic redox conditions control late Ediacaran ecosystems in
690 the Nama Group, Namibia. *Precambrian Res.* 261, 252–271.
691 Zhang, F., Xiao, S., Kendall, B., Romaniello, S.J., Cui, H., Meyer, M., Gilleaudeau, G.J.,
692 Kaufman, A.J., Anbar, A.D., 2018. Extensive marine anoxia during the
693 terminal Ediacaran Period. *Sci. Adv.* 4, eaan8983.
694 <https://doi.org/10.1126/sciadv.aan8983>
695
696

697 **Figure captions**

698 **Figure 1:** Top panel: The range of $\delta^{238}\text{U}$ for different sources and sinks in the modern
699 uranium cycle (Andersen et al., 2017, 2014; Stirling et al., 2007; Tissot and Dauphas,
700 2015; Weyer et al., 2008). Pale boxes define the potential range of values and solid
701 boxes suggest the most likely value. Middle panel: The $\delta^{238}\text{U}$ of organic rich
702 mudrocks in the Doushantuo Formation (Kendall et al., 2015), and the inferred $\delta^{238}\text{U}$
703 of seawater ($\delta^{238}\text{U}_{\text{sw}}$) using a fractionation factor between seawater and anoxic
704 sediments (Δ_{anox}) of 0.6‰. Bottom panel: The $\delta^{238}\text{U}$ of carbonates from the Nama
705 Group (this study), assumed to directly represent $\delta^{238}\text{U}_{\text{sw}}$, and the inferred $\delta^{238}\text{U}$ of
706 the anoxic sink, assuming Δ_{anox} of 0.6‰.

707

708 **Figure 2:** Panels ordered left to right: Stratigraphic log, $\delta^{13}\text{C}$ (green circles), U/Ca
709 ratios (orange circles) and $\delta^{238}\text{U}$ (blue circles) for carbonate rocks from Kuibis
710 Subgroup of the Nama Group. The local distribution of biota within the section is
711 marked on the stratigraphic log. The $\delta^{238}\text{U}$ of modern seawater (blue line) is shown
712 for comparison. The average $\delta^{238}\text{U}$ (dashed grey line) is calculated as an average of
713 all data in the upper Omkyk and Hoogland Members, excluding one anomalously
714 enriched value.

715

716 **Figure 3:** Comparison of $\delta^{13}\text{C}$ and $\delta^{238}\text{U}$ from the Nama Group, Namibia (this study),
717 with two independent carbonate sections of the Dengying Formation, south China
718 (Wuhe and Gaojiashan) (from Zhang et al., 2018b). The trend from modern marine
719 $\delta^{238}\text{U}$ (black dashed line) towards low $\delta^{238}\text{U}$ of -0.8 to -1.0‰ (grey line) is apparent in
720 all three sections, in both limestone and dolostone. The stratigraphic log for
721 Gaojiashan is based on Cui et al., (2016). The recorded range of the Nama

722 Assemblage is indicated on the stratigraphic log, with dashed lines indicating that the
723 range extends below the base of the section.

724

725 **Figure 4:** Compilation of limited $\delta^{238}\text{U}_{\text{SW}}$ inferred from Neoproterozoic and
726 Cambrian rocks (Dahl et al., 2014; Kendall et al., 2015; Lau et al., 2017; Wei et al.,
727 2018; Zhang et al., 2018). The transition from a modern marine $\delta^{238}\text{U}_{\text{SW}}$ to much
728 lower $\delta^{238}\text{U}_{\text{SW}}$ ~550 Ma coincides with the end of an inferred ‘ocean oxygenation
729 event (OOE)’ (pale blue panels, Sahoo et al., 2016). Data from Kendall et al., (2015)
730 has been replotted as $\delta^{238}\text{U}_{\text{SW}}$ using an assumed U isotope fractionation factor
731 between anoxic sediments and seawater of 0.6‰, consistent with Kendall et al.
732 (2015). Global or expansive periods of glaciation are also marked in purple.

733

734 **Figure 5: a)** Model results for the $\delta^{238}\text{U}_{\text{SW}}$ resulting from a given percentage of anoxic
735 seafloor based on $\Delta_{\text{anox}} = 0.6\text{‰}$ and $\delta^{238}\text{U}_{\text{riv}}$ of -0.30‰ . A lower $\delta^{238}\text{U}_{\text{riv}}$ of -0.34‰
736 results in a smaller estimate of seafloor anoxia, and a higher $\delta^{238}\text{U}_{\text{riv}}$ of -0.26‰ results
737 in a larger estimate of seafloor anoxia. **b)** For lower Δ_{anox} , a greater increase in
738 seafloor anoxia (F_{anox}) is required to reproduce $\delta^{238}\text{U}_{\text{SW}}$ of -0.81‰ recorded in the
739 Nama Group. The average $\delta^{238}\text{U}$ recorded in the Dengying Formation, south China, is
740 shown for comparison (Zhang et al., 2018).

741

742

743

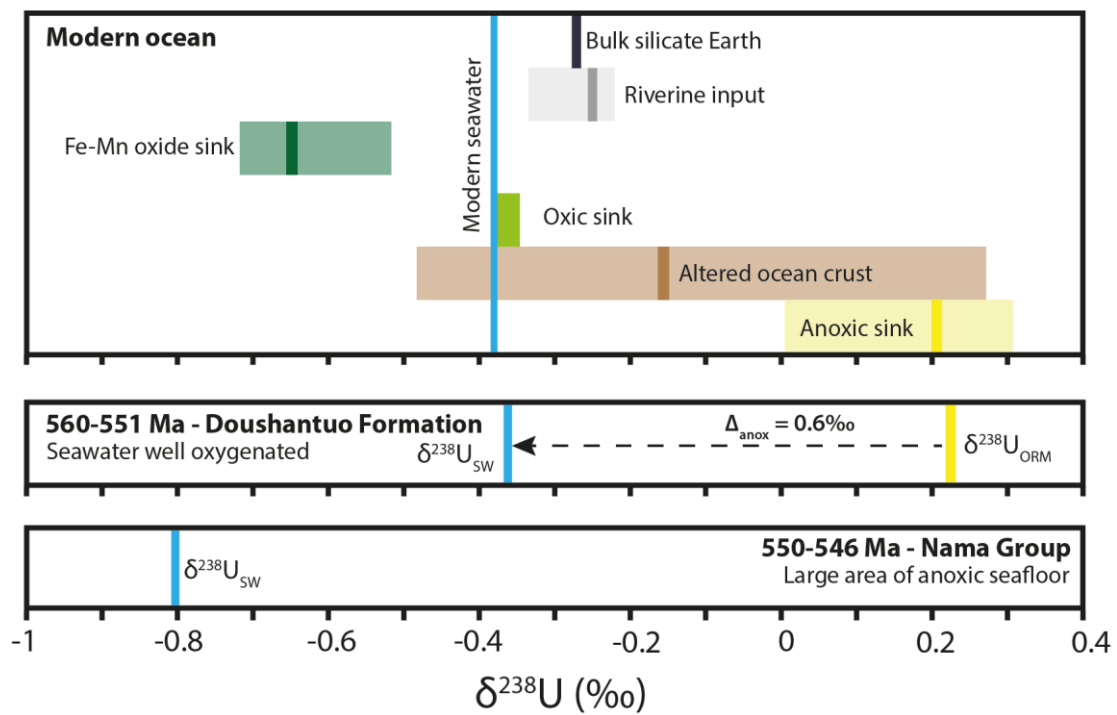
744

745

746

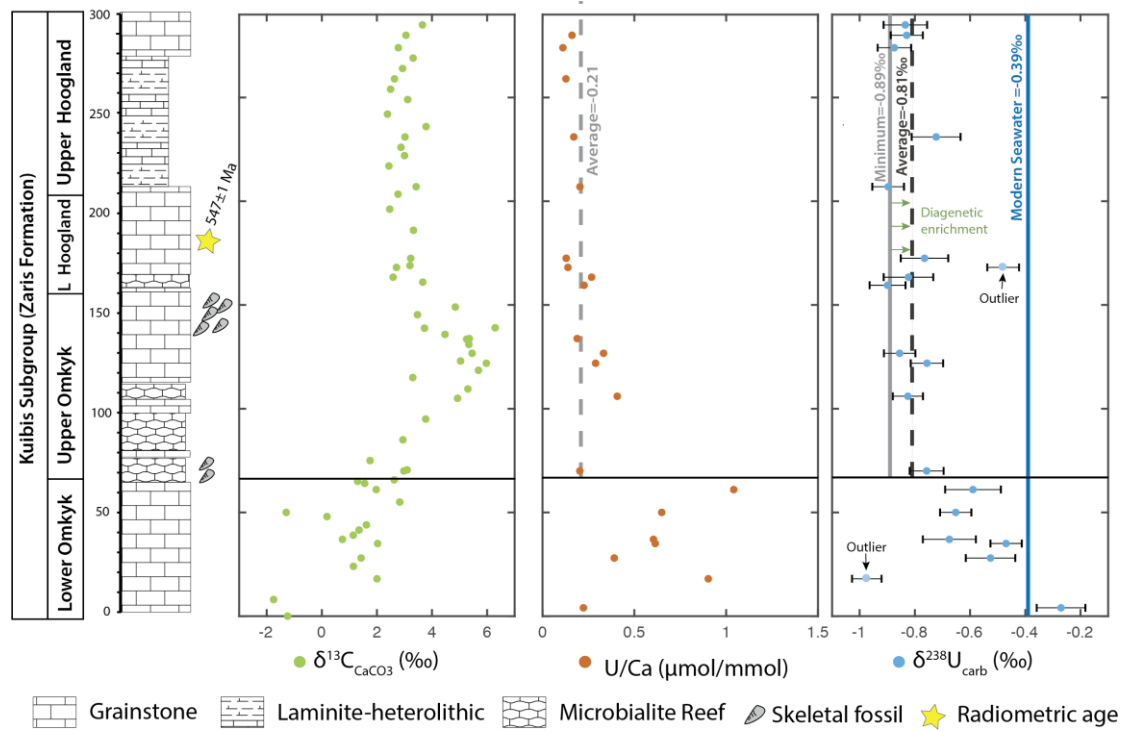
747 **Figure captions**

748 **Figure 1:**



749

750 **Figure 2:**



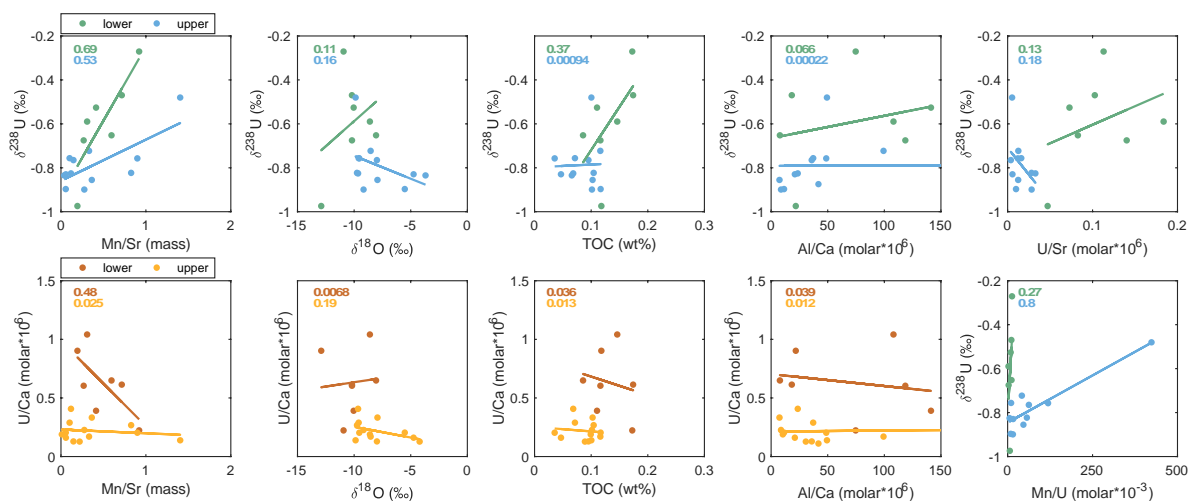
751

752

753

754

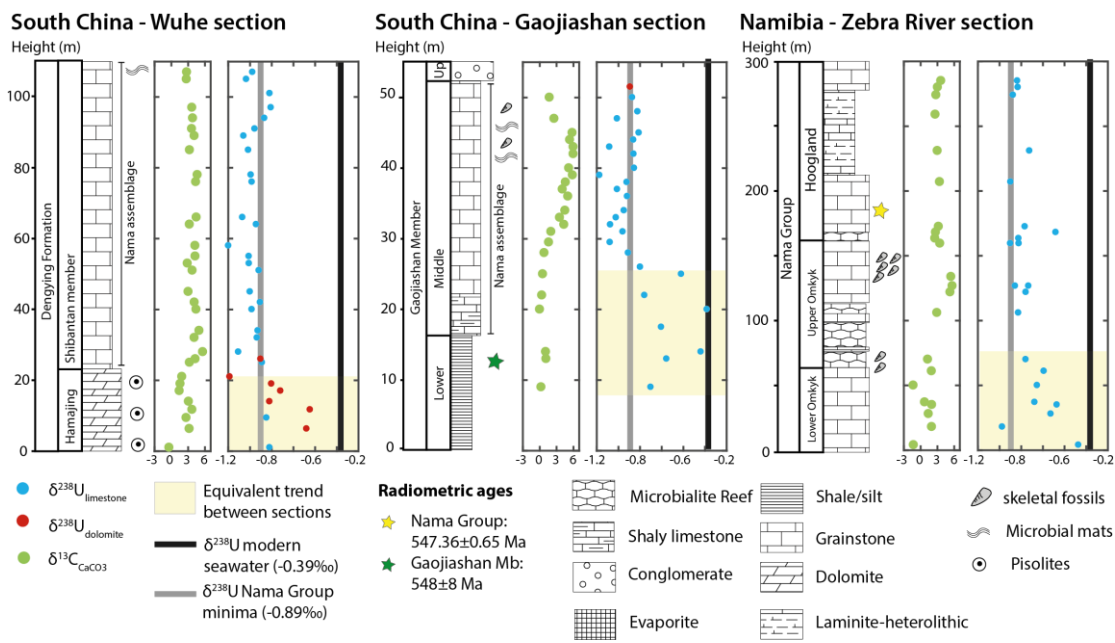
755 **Figure 3:**



756

757

758 **Figure 4:**



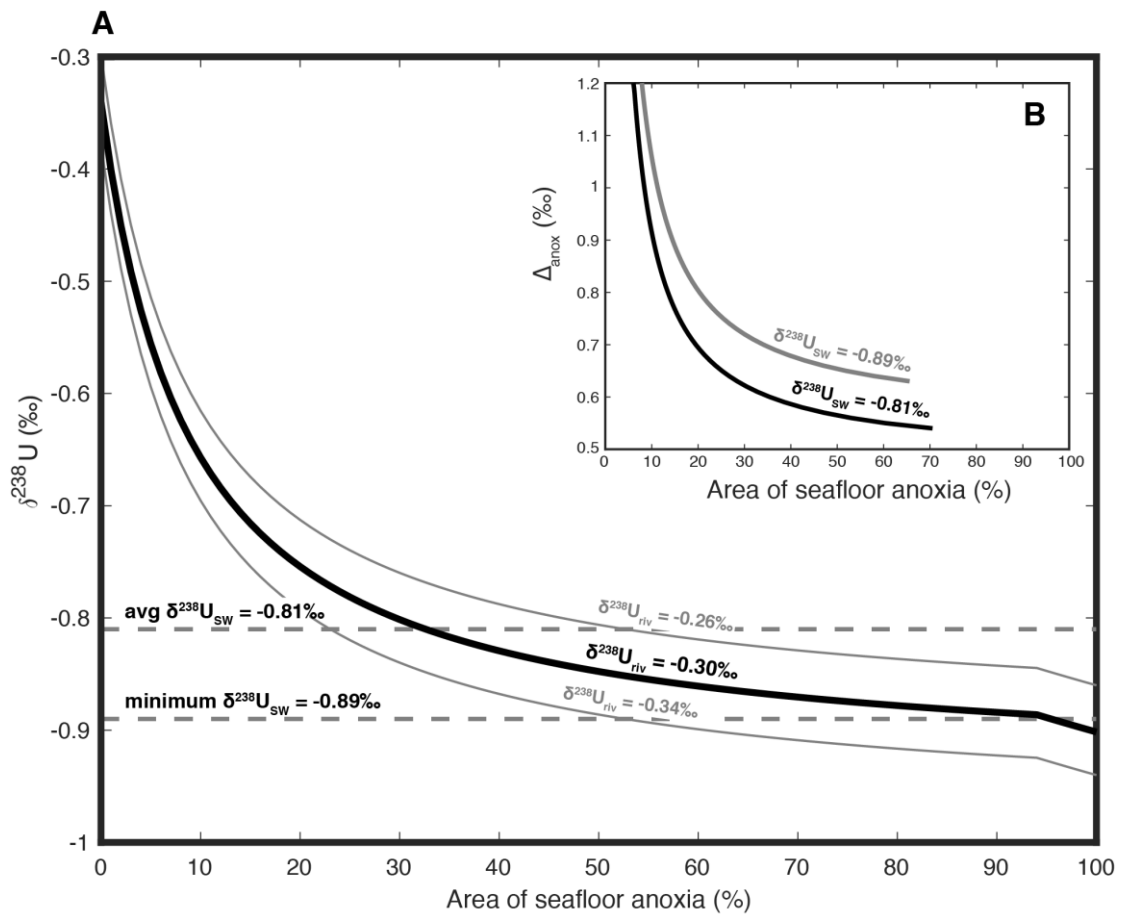
759

760

761

762

763 **Figure 5:**



764

765